Experimental characterization of a nonlinear hydraulic engine mount

Mayank Tiwari,[a] Haryanto Adiguna,[a] and Rajendra Singh[a]

(Received 2002 January 29; revised 2002 November 05; accepted 2002 November 15)

Hydraulic engine mounts exhibit nonlinearities due to internal fluid flow characteristics, compliances of elastomeric fluid chambers, decoupler switching mechanisms, and vacuum formation. To quantify these nonlinearities, several new or refined bench experiments are first proposed. Then steady state dynamic tests are conducted on an elastomer test machine where the transmitted force and top chamber pressure signals are acquired and analyzed. Various configurations of the mount are modeled and simulated to yield the steady state behavior at different frequencies and amplitudes of displacement excitation. Both frequency and time domain simulations agree well with measurements. © *2003 Institute of Noise Control Engineering.*

Primary subject classification: 46.2; Secondary subject classification: 46.1

1. INTRODUCTION

A non-resonant dynamic testing method is often used to characterize rubber and hydraulic mounts, bushings and other vibration isolators.[1] In such a test, sinusoidal displacement $x(t) = X \sin(2\pi ft)$ with an amplitude X (or peak to peak value of $2X$) is applied at frequency f (Hz). The isolator is always under a preload F_m that produces a mean or time-invariant displacement x_m. The dynamic response is characterized by the force transmitted $F_T(t)$ into a rigid base, as shown in Fig. 1a. Typically, the Fourier filter is used so that $F_T(t) = |F_T| \sin(2\pi ft + \phi)$ is measured only at the frequency of excitation f, while ignoring super and sub-harmonics of f.[2-4] One may then define complex-valued dynamic stiffness $\tilde{K}(f,X) = Ke^{i\phi}$ where $K = |F_T| / X$ is the dynamic stiffness modulus and ϕ is the loss (phase) angle. Though this characterization method works well for product specification and quality control, it is not sufficient to clearly identify the mount parameters that may be used to construct mathematical simulation models of the governing physical system. The rubber mount case may be assumed to be described by a Voight type visco-elastic model, as shown by k_r and b_r elements in Fig. 1b with $u(t,x) = 0$.[5] Given the elastomer nonlinearity, k_r and b_r will be amplitude (X) and frequency (f) dependent though such variations are negligible compared to the properties exhibited by hydraulic mounts. Therefore, we assume that k_r and b_r are constant over the lower frequency regime, say up to 50 Hz. In contrast, hydraulic mounts are highly amplitude dependent devices and their parameters show considerable variations with the frequency of excitation. Figure 1b shows the hydraulic path via the time-varying and nonlinear hydraulic reaction force $u(t,x)$. In order to develop simulation models and predictive design tools, $u(t,x)$ must be experimentally characterized and the associated system parameters have to be fully identified.[2-4,6] This is the main focus of this paper.

2. PROBLEM FORMULATION

A. Example case

A schematic of a passive hydraulic mount is shown in Fig. 2. In practice, one may use 3 to 4 mounts out of which one is typically a hydraulic mount. The device is mounted to the automotive engine through the top mounting studs (1) and to the vehicle chassis through the bottom mounting studs (2). Metal inserts (3, 6) are molded into the elastomeric element (4) so that the compression and shear deformations of the

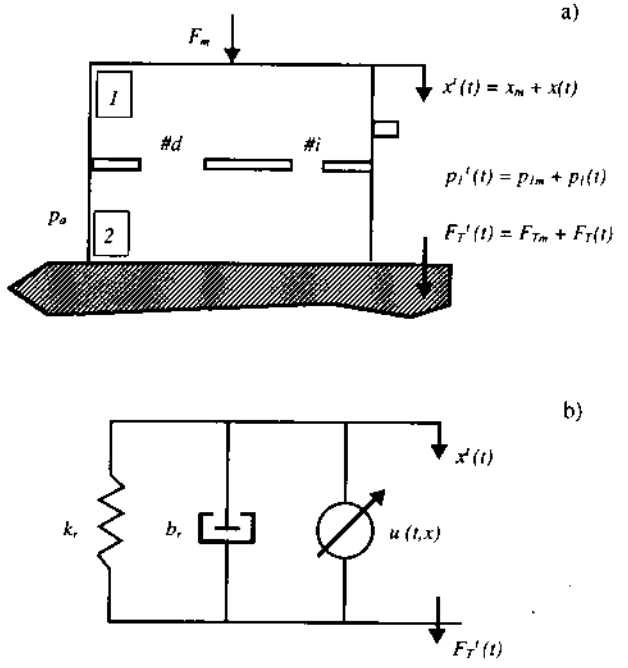

c)

Variable	+	−
$x^t(t)$	↑	↓
$p_i^t(t)$	Compression	Expansion
$F_T^t(t)$	↑	↓
$q_d(t)$	↑	↓
$q_i(t)$	↑	↓

Fig. 1– Hydraulic mount concept. (a) Measured variables, (b) Force transmission paths, and (c) Sign convention where ↑ implies an upward motion and ↓ refers to the downward motion.

[a] *Acoustics and Dynamics Laboratory, Center for Automotive Research, The Ohio State University, 206 West 18th Ave., Columbus, Ohio 43210-1107 USA. E-mail: singh.3@osu.edu.*

Singh_124

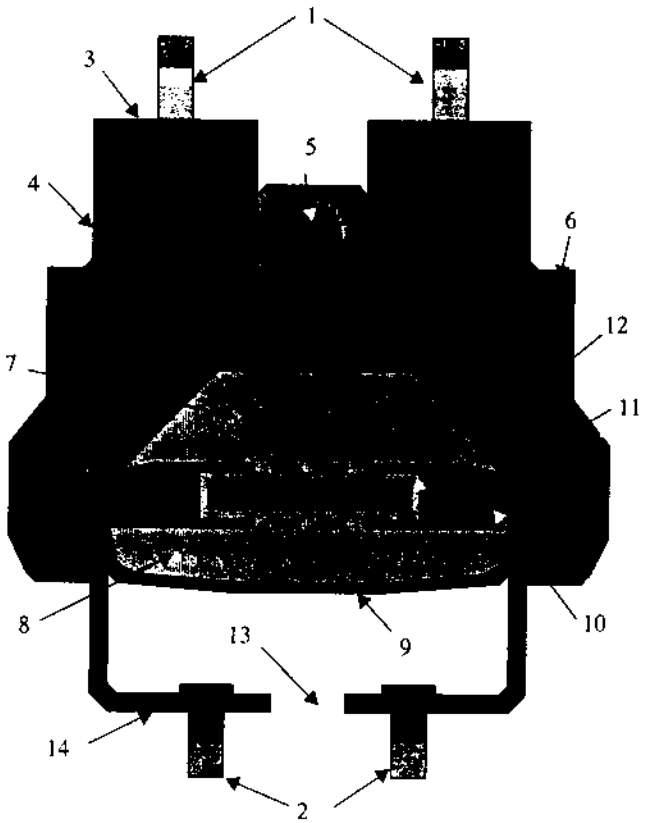

Fig. 2– Passive hydraulic mount. See Section 2A for the identification of components.

elastomeric element provide stiffness to support the static engine weight. The pin (5) acts as a stopper for preventing excessive tension in the top chamber for very large tensile displacements. The top (7) and bottom (8) chambers are filled with an anti-freeze and water mixture.[4] When the top chamber is compressed, liquid is forced to flow through the two fluid channels in the orifice plate (10): (a) an inertia track (11), which is a long narrow channel to provide the fluid damping, and (b) a decoupler (12) with a wider orifice along with a free floating elastomeric disk. The flexible rubber diaphragm (9) acts as an accumulator as the fluid flows from the top to the bottom chamber. The air breather (13) allows the air to escape from the base plate (14) so that ideally there is no additional compliance incorporated by the entrained air.

B. Static analysis

Figure 1a shows the top (#1) and bottom (#2) fluid chambers. Total force transmitted $F_T^t(t)$ by the hydraulic mount is as follows where A_p is the effective piston area in the top chamber, p_1 and p_2 are the top and bottom chamber pressures, p_a is the ambient pressure, $\dot{x}$ is the velocity, and the superscript t implies the total variable.

$$F_T^t(t) = F_{Tm} + F_T(t) = k_r x^t(t) + b_r \dot{x}^t(t) + A_p[p_1^t(t) - p_2^t(t)] + A_p[p_2^t(t) - p_a] \quad (1)$$

Mean (with subscript m) and dynamic components of $F_T^t(t)$ are as follows where one may assume that $p_{1m} = p_{2m} \cong p_a$ though p_{1m} depends on F_m as shown later.

$$F_{Tm} = F_m = k_r x_m + A_p(p_{1m} - p_a) \quad (2)$$

$$F_T(t) = k_r x(t) + b_r \dot{x}(t) + A_p p_1(t) \quad (3)$$

Our sign convention will be consistent with those employed by commercial test machines.[1] Accordingly, the upward action of $x^t(t)$ is positive, and the tensile forces (F_m and F_T^t) are positive. Under the preload (compressive or negative mean force F_m), the fluid chamber pressure p_1^t will increase and hence p_1^t is positive in the compression mode; consistent with the Hooke's law for fluids that defines the bulk modulus.

C. Dynamic model

The hydraulic mount is modeled by lumping the fluid system into several control volumes as shown in Fig. 3.[2,3] The system linearized parameters for a free decoupler include the fluid compliances (C_1 and C_2), elastomeric element stiffness (k_r) and damping (b_r), inertia track inertance (I_i) and resistance (R_i), and decoupler resistance (R_d). However, Kim and Singh have shown via experimental measurements that C_1, C_2, R_i and R_d have nonlinear characteristics.[2,3,6] Based on conservation of mass, nonlinear governing equations are derived from the model of Fig. 3.

$$q_i(t) + q_d(t) = A_p \dot{x}(t) - C_1(p_1)\dot{p}_1(t) \quad (4)$$

$$-q_i(t) - q_d(t) = C_2(p_2)\dot{p}_2(t) \quad (5)$$

where q_i and q_d are the flow rates through the inertia track and decoupler respectively. Note that these can be related to R_i and R_d for linear fluid resistance elements. Further, $C_1(p_1)$ and $C_2(p_2)$ denote nonlinear compliances. The fixed decoupler case[2] can be easily analyzed as a sub-set by inserting $q_d = 0$ or $R_d \to \infty$ in the expressions for a free decoupler case.

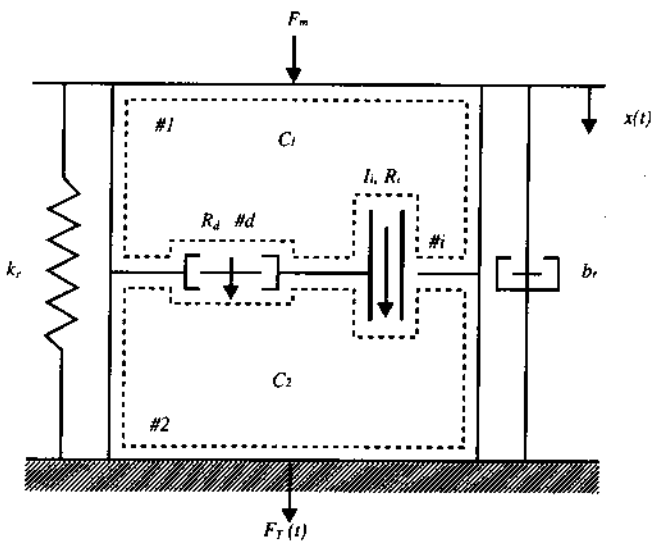

Fig. 3– Lumped parameter model of a free decoupler mount and linearized parameters.

D. Scope and objectives

The primary objective of this article is to suggest experimental methods that must be adopted in order to truly identify the nonlinear parameters or phenomena of a typical hydraulic mount. The scope of this study is however limited to the steady state behavior up to $f = 50$ Hz given peak-to-peak (pp) amplitudes (i.e. $2X$) from 0.3 to 3.0 mm. Specific objectives are to: (1) Measure A_p, and p_{1m} vs. F_m relationships; (2) experimentally determine p_1–V_1 and p_2– V_2 relationships for both chambers; (3) examine the vacuum phenomenon and associated asymmetric C_1 nonlinearity; (4) measure the q_i vs. $\Delta p = p_1 - p_2$ relationship for steady flow; (5) develop and validate a nonlinear simulation model; and (6) examine the existence of sub and super harmonics of f. The only prior article that addresses some of these objectives is by Kim and Singh who designed several bench experiments and developed relevant nonlinear models in the early 90's.[6] Our work is an extension of this study though we have designed new experiments, equipped these with modern instrumentation, and refined experimental procedures. Also, note that the hydraulic mount designs have changed to some extent over the last decade and therefore new experiments must be conducted to characterize their nonlinear behavior.

3. STATIC MEASUREMENTS

The preload F_m affects the mount operating point in two ways. First, it dictates the chamber pressure operating point about which linear or nonlinear parameters are to be estimated. Thus the effect of F_m on $\tilde{K}(f,x)$is significant. Second, it determines $\langle p_1'(t) \rangle_t$, which affects the entire fluid system where $\langle\ \rangle_t$ implies a true time average. Kim and Singh assumed that $\langle p_1'(t) \rangle_t$ and p_{1m} are the same static pressures.[2] Figure 4a shows the measured p_{1m} as a function of F_m. Notice that since the bottom chamber is very compliant, the fluid pressure remains at about p_a when F_m is less than 1000 N. The top chamber acts like a piston under dynamic conditions, and its effective area A_p determines the fluid displaced under static or dynamic conditions. Also, the F_T' expression is a function of A_p. The effective area is determined experimentally by applying a precise static displacement, x_m, on the top chamber only. The entire set up is connected to a rigid base; also the tubing must be very stiff. The compliance measurement is made by placing the mounts within the dynamic elastomer test machine. The volume displaced (ΔV) changes the height (Δh_G) of colored water in a connected sight glass of area A_G. Thus, $\Delta V = A_p x_m = A_G \Delta h_G$. Figure 4b shows the measured ΔV vs. x_m data and the corresponding linear curve-fit. The area A_p is obviously related to its slope; it is virtually a constant value under varying displacements.

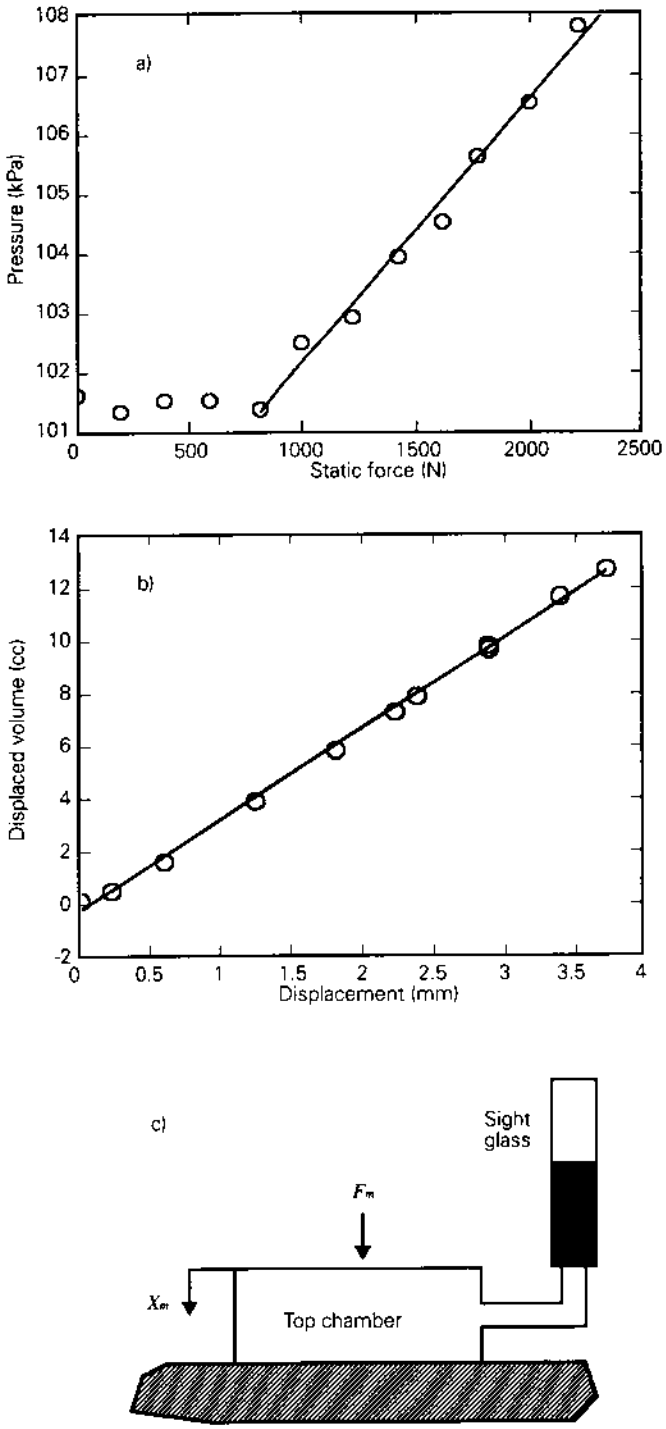

Fig. 4– Static measurements. (a) p_{1m} vs. F_m, (b) Effective piston area A_p of top chamber (Key: O Measured data, — Linear curve-fit), and (c) Effective piston area measurement setup.

4. NONLINEAR COMPLIANCE MEASUREMENTS

Linear compliance of a fluid chamber is defined by $C = dV/dp \approx \Delta V/\Delta p$ where ΔV is the volume decrease and Δp is the pressure applied about an operating point. For a nonlinear element, the p–V curve is measured with a bench experiment similar to the one reported by Kim and Singh,[6] and the linearized compliance is evaluated at a given operating point. However, unlike Kim and Singh,[6] we estimate the compliance with a given preload F_m. For the top chamber, the test is conducted for $F_m = 0$, 800 and 1200 N; the $F_m = 0$ N case was

previously analyzed by Kim and Singh.[6] The preload was applied by the elastomer system under manual static control.[1] Measured results of Fig. 5a and Table 1 show that the C_l values under 800 and 1200 N preloads are about the same; but C_l is much higher with $F_m = 0$. From the simulation results shown later, it is seen that the K and ϕ predictions match when C_l is about 2×10^{-11} to 3×10^{-11} m^5/N. Therefore, a nominal value of 2.5×10^{-11} m^5/N is used for simulation. Figure 5b shows that the bottom chamber compliance is quite nonlinear and that it exhibits some hysteresis due to loading and unloading. Given the non-linear p–V relationship, we could either linearize the curve at an operating point or curve-fit it using a polynomial nonlinear model. For the bottom chamber, a third order fit is found to be sufficient. Also, note that the bottom chamber pressure typically stays almost constant due to a very compliant rubber diaphragm, i.e. $p_2 \cong p_a$. Thus, the linearization yields a good approximation for C_2.

The vacuum phenomenon observed in the top chamber is poorly understood though it was briefly reported by Kim and Singh.[6] A certain volume of gas can be assumed to be dissolved in the fluid but this comes out under a reduced pressure depending on the ambient temperature as well as the dynamic excitation conditions that are difficult to quantify. Under vacuum conditions, Kim and Singh used the ideal gas law to determine a theoretical p–V relationship.[6] Since it is not easy to determine the amount of pre-dissolved gas, measured dynamic data is employed to estimate the p–V relationship. With reference to Fig. 1a, a pressure transducer is installed in the top chamber. Under the sinusoidal test, we measure the $p_l(t)$ time history. Intuitively, it can be said that vacuum formation in the top chamber results in an increase in C_l. Also, note that the bottom chamber pressure typically stays almost constant due to a very compliant rubber diaphragm i.e. $p_2 \cong p_a$. The net dynamic stiffness characteristics of the mount are then given by K_l under compression ($p_l > p_a$) and by K_v under expansion ($p_l < p_a$). The mount should thus behave as a nonlinear system with a bi-linear stiffness curve as shown in Fig. 6a. Measured pressure results show a distortion in $p_l(t)$ as illustrated by Fig. 6b. The pressure amplitude reduces from p_l' (without vacuum) to p_v' (under vacuum) under sinusoidal tests as shown in Fig. 6b. The amplitude ratio is related to the

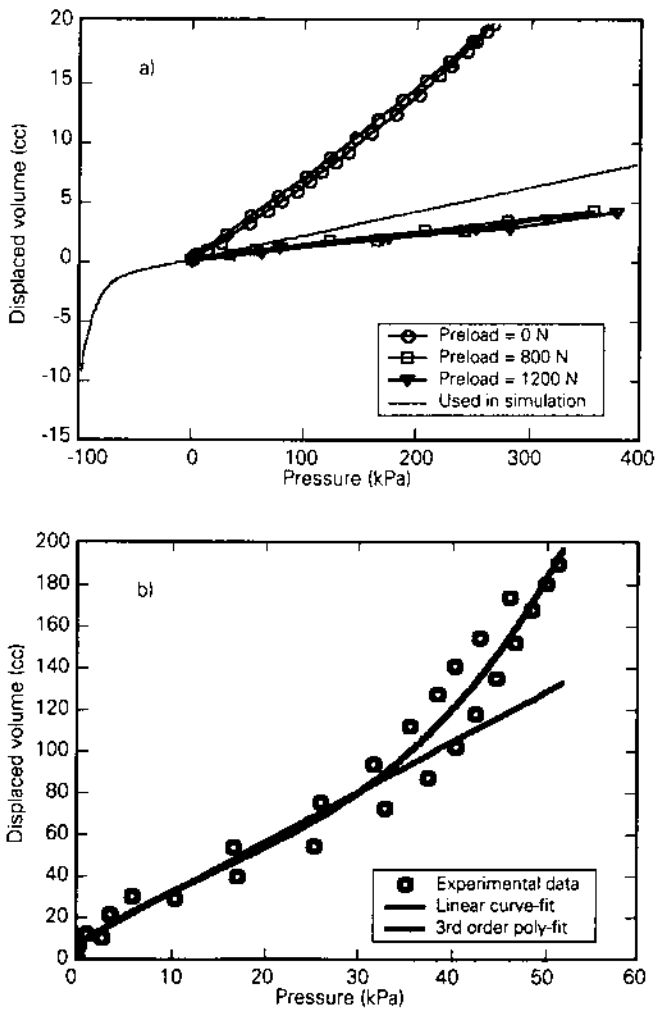

Fig. 5– Nonlinear compliance curves. (a) Top chamber and (b) Bottom chamber.

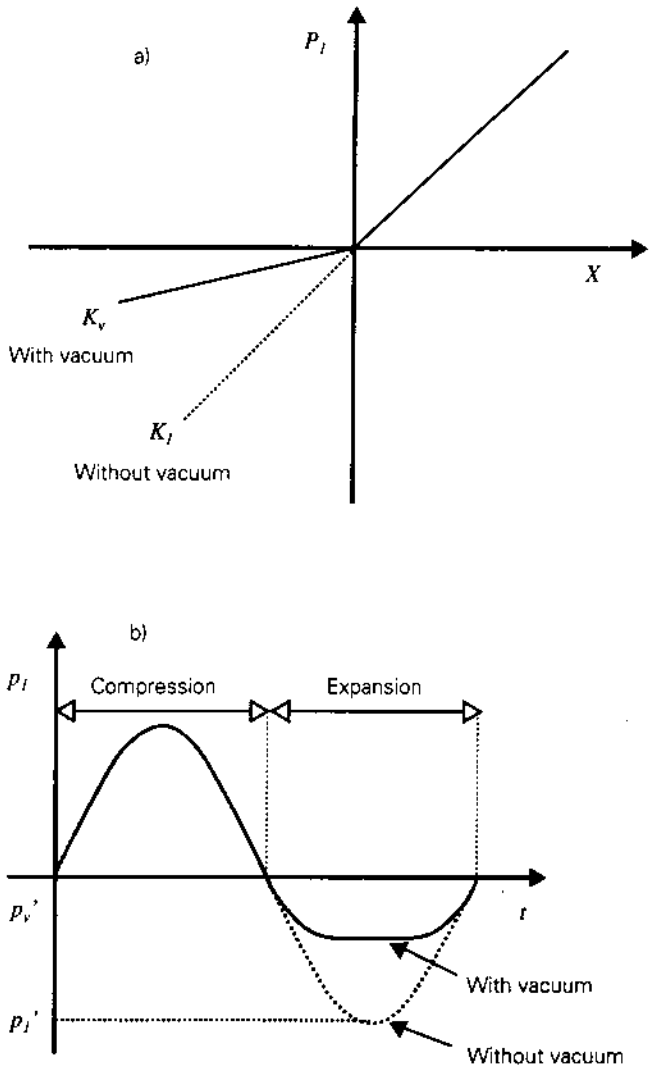

Fig. 6– Effect of vacuum on p_l. (a) Asymmetric stiffness characteristics of top chamber and (b) Distortion in the $p_l(t)$ waveform.

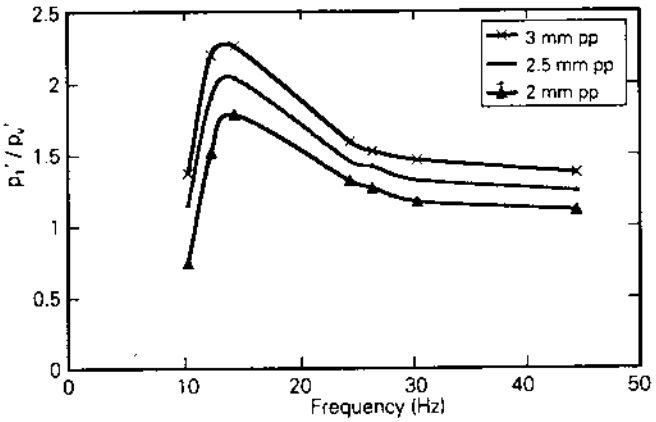

Fig. 7– Measured pressure distortion due to vacuum formation.

relative stiffness (or compliance) of Fig. 6a as follows, where the subscript v implies under vacuum conditions

$$\frac{p_1'}{p_v'} \cong \frac{K_1}{K_v} \cong \frac{C_v}{C_1} . \qquad (6)$$

Figure 7 shows the measured pressure amplitude distortion ratios over a wide range of frequencies for X = 1.0, 1.25, and 1.5 mm. The resulting spectra suggest an amplitude-dependent softening nonlinearity. The bi-linear stiffness curve of Fig. 6a appears to be discontinuous at the origin. However, experimental results of $p_i(t)$ show that the transition is rather gradual and therefore a smooth curve is used in the simulation model as shown in Fig. 5a. Next assume the nonlinear model of compliance (Fig. 7) as follows: $C_1(p_1) = dV_1/dp_1 = ap_1^n + b, P_1 \leq P_a$ where n is the polytropic coefficient. Based on measurements, n is estimated to be in the range of 12–30. The coefficient a is 10^{-60} and b is the slope of the V–p curve under atmospheric conditions given zero gauge pressure. Further analysis of the vacuum phenomenon is beyond the scope of this paper.

5. INERTIA TRACK RESISTANCE MEASUREMENTS

The orifice plate positioned between the top and bottom chambers is the main mechanism that controls the fluid system characteristics. Typically, this plate consists of two parts as shown in Fig. 5: (a) the top orifice plate that holds the decoupler and provides the fluid channel for the inertia track, and (b) the bottom orifice plate that provides the entrance/exit passages for the decoupler and inertia track as well as a mechanism for closing the top orifice plate so that no leaking occurs. Measured properties are listed in Table 1. The inertia track of Fig. 8a is a long and spiral channel and its inertance is given by I_i. Due to its geometry, the inertia track has high resistance (R_i) that results in sufficient damping needed to control engine resonances. The inertia track is modeled via a first order fluid system differential equation, where the fluid compliance is neglected.

Note that Eq. (7) is non-linear because of the R_i term.

$$I_i\dot{q}_i(t) + R_i(\Delta p_{12}, q_i)q_i(t) = p_2(t) - p_1(t) . \qquad (7)$$

The I_i term plays an important role in the model but its measurement is very difficult since it requires a non-zero $\dot{q}$ with a zero q and a zero $\dot{p}$. Furthermore, an accurate estimate based on partial differential equations would require a complicated and lengthy analysis. The simplest approximation is to assume the flow to be one-dimensional and steady, and to treat the inertia track as a straight pipe of length l_i and area A_i. The inertance is $I_i = \rho_f l_i/A_i$ where ρ_f is the fluid density. Note that a range between I_i and 1.33 I_i could be considered despite the non-uniform velocity profiles and other complications due to turbulent flow. Thus, at worst a 33% error is expected.[7]

In general, the relationship between steady state pressure drop (Δp) and flow rate (q) in a pipe is nonlinear. Measured results of Fig. 9 for water and anti-freeze mixtures verify this for the inertia track where Δp_{12} is determined to be a function q_i^2. Assuming laminar flow in a capillary tube, the inertia track resistance can be calculated using the following formula[7]

$$R_i = 128\,\mu l_i/\pi d_i^4$$

where μ, l_i, and d_i denote the fluid viscosity, length, and hydraulic diameter. Table 1 shows that this formula underestimates the resistance. This is expected since it neglects the end effects and pressure losses due to cornering. The non-linear relationship between q_i and Δp_{12} is given by the sharp-edged orifice formula

$$q_i = C_d A_i \sqrt{2\Delta p_{12}/\rho_f}$$

where C_d is the coefficient of discharge. This nonlinear approximation matches quite well with measured results. Assuming turbulent flow, the value of C_d = 0.61 can be used as a good approximation.[7] The R_i is determined by measuring Δp_{12} across the inertia track. Utilizing a centrifugal pump, a steady-state flow q_i is generated and passed through the inertia track fixture in which the decoupler is blocked. The volumetric flow rate q_i is measured using an electromagnetic flow meter, whereas Δp_{12} is measured using a differential pressure transducer.[6]

6. DECOUPLER MODELS

As illustrated in Fig. 8b-c, the decoupler itself is a thin rubber disk of diameter d_d and thickness t_d. The decoupler is blocked by the top orifice plate on one side and by the bottom orifice plate on the other side. Between the decoupler and the top orifice plate internal wall, there is a small clearance c_d. This allows the decoupler to move freely where δ_d is the net decoupler gap, as shown in Fig. 8c. In our mount, 7 small holes expose the decoupler to the top and bottom chambers. To simplify our analysis, the first approach eliminates the decoupler mechanism; the flow then takes place only through the inertia track. To do this experimentally, the decoupler is fixed to the orifice plate using hard epoxy so that $q_d = 0$. The adhesive material must be sufficiently rigid so as not to introduce any additional compliance. For the case of a free-floating decoupler, the fluid flow is controlled by the decoupler switching mechanism that couples or decouples the inertia track. When the disk floats in the middle of the gap, it will

TABLE 1– Measured or identified mount parameters.

a. Measured orifice plate geometry

Inertia track: l_t = 236 mm, A_t = 84 mm²

Decoupler: d_d = 50 mm, A_d = 1960 mm², δ_d = 1 mm, t_d = 4 mm, H_d = 122 mm²

b. Predicted and measured chamber compliance results

Top Chamber Compliance		
Above p_u	F_m = 0 N	$C_1 = 7.29\times10^{-11}$ m³/N
	F_m = -800 N	$C_1 = 1.05\times10^{-11}$ m³/N
	F_m = -1200 N	$C_1 = 1.09\times10^{-11}$ m³/N
Below p_u	$C_1 = -7\times10^{-45}\, p_1^{7} + 2.5\times10^{-11}$	
Bottom Chamber Compliance		
Linearization		$C_2 = 2.4\times10^{-4}$ m³/N
Third Order Polynomial-fit		$C_2 = 1.51\times10^{-18} p_2^{3} - 6.82\times10^{-14}$ $p_2^{2} + 3.13\times10^{-9}\, p_2 + 5.19\times10^{-6}$

c. Predicted and measured inertia track resistance R_t

Predicted	Capillary Tube Formula	$R_t = 8.65\times10^{6}$ N-s/m⁵
	Sharp-edged Orifice Formula	$R_t = 1.90\times10^{11}\, q_t$ N-s/m⁵
Measured	Linearization (at q_t = 1×10^{-4}m³/s)	$R_t = 3.45\times10^{7}$ N-s/m⁵
	Second Order Poly-fit	$R_t = 3.45\times10^{11}\, q_t$ N-s/m⁵

provide a very small fluid resistance R_d as compared to R_t. On the other hand, while it bottoms out either at the top or bottom, q_d is zero, and thus the total flow $q = q_t$. A linear model of the decoupler is given by a first order differential equation (8) where b_v, m_d, A_d, and x_d denote the viscous damping coefficient, mass, cross-sectional area, and displacement of the disk, respectively,

$$m_d\ddot{x}_d(t) + b_v\dot{x}_d(t) = A_d\left[p_2(t) - p_1(t)\right]. \qquad (8)$$

The flow rate through the decoupler is then modeled by the equation $q_d(t) = A_d\dot{x}_d(t)$ where x_d is from 0 to $\delta_{d1}+\delta_{d2}$. The switching mechanism will be explained in the next section. The b_v term is difficult to estimate experimentally as it would require the measurement of transient flow while controlling $x_d(t)$. Measured $\tilde{K}(f,x)$ results do show high damping that is introduced by the decoupler. Colgate et al. suggested that the squeeze film damping force F_s opposes the decoupler when it is about to close.[4] Assuming that there is no opening in the decoupler plate, F_s is defined as:[8] $F_s = b_s\dot{x}_d$ where $b_s = 3\mu r_d/2\Delta^3$ and μ, r_d, and Δ denote fluid viscosity, decoupler radius, and the remaining gap between the decoupler and the top (or bottom) orifice plate as the decoupler is about to close at the top or bottom, respectively. Assuming a linear velocity profile, steady flow, and constant μ, the viscous damping force F_v due to the shear stresses acting on the side of the decoupler can be defined as:[9] $F_v = b_v\dot{x}_d$ where $b_v = \mu A_v / c_d$ and A_v is the effective force area.

Figure 10 compares the squeeze film and viscous damping constants as a function of Δ. Observe that b_v is very small, of

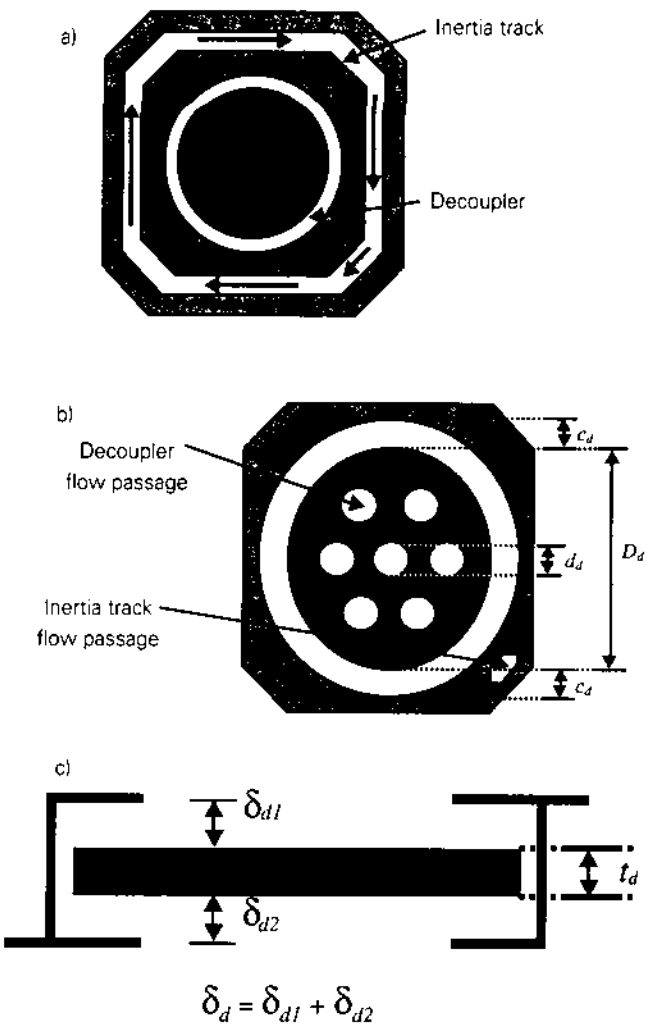

Fig. 8– Orifice plate. (a) Top plate with inertia track, (b) Bottom plate with decoupler, and (c) Decoupler disk and clearance.

the order of 10^{-2} (N-s/m), while b_s ranges from ∞ to 10^{0} (N-s/m). A parametric study was conducted, and it was seen that the simulation matches experiments very well when the effective viscous damping value of b_{ve} = 100 N-s/m is selected.

7. DYNAMIC CHARACTERIZATION TESTS

The objective of dynamic tests is to study the response of the hydraulic mount when it is subjected to steady state sinusoidal excitations. Two configurations of a take-apart mount are used for dynamic study: (a) complete mount with free decoupler and inertia track, and (b) fixed decoupler mount with only the inertia track. The take-apart mount comprises top and bottom chambers, and an orifice plate with inertia track and decoupler. The assembly is done with a clamping fixture in a water bath. Care must be taken that there are no air bubbles in the water bath that can be trapped during the assembly. For maintaining a low level of dissolved air, the water temperature should be low. The internal dynamics of the mount and especially the instantaneous stages of decoupler are studied by installing a pressure transducer in the top

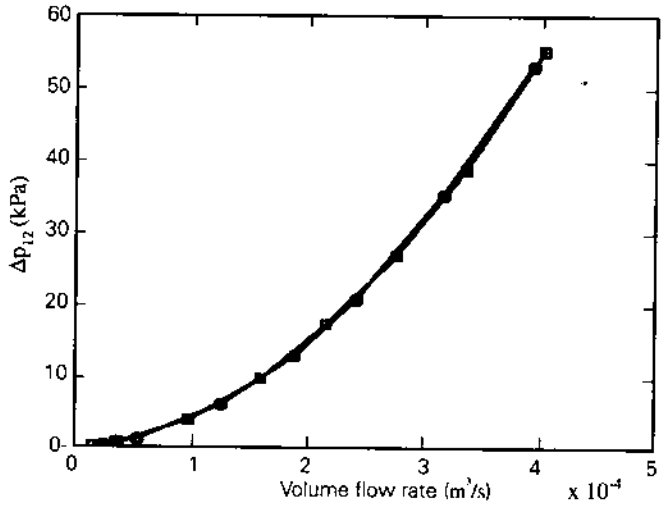

Fig. 9– Nonlinear resistance characteristics of inertia track. Key: O Water, — Anti-freeze mixture.

chamber. Two kinds of pressure transducers were used for experimentation: (i) an absolute pressure transducer (strain gage type) for $p_1'(t)$, and (ii) a dynamic pressure transducer (piezoelectric) for $p_1(t)$. The absolute pressure transducer is primarily used for recording the p_{1m}, while the dynamic pressure transducer is used for recording the $p_1(t)$ accurately.

Under static manual control of the machine controller, the mount was subjected to a specific F_m, and p_1m is recorded from the absolute pressure transducer. This gave an estimate of the initial pressure to be used in the simulation model. The elastomeric components of the mount (k_r and b_r) are also obtained when the fluid is completely drained out from the mount and by removing the lower chamber so as not to have any air accumulation effect. Compared to a typical hydraulic mount, the $K(f,x)$ and $\phi(f,x)$ values of the elastomeric element are very low and stay almost invariant at lower frequencies. Finally, the measured raw signals $x(t)$, $F_T(t)$, and $p_1(t)$ are taken

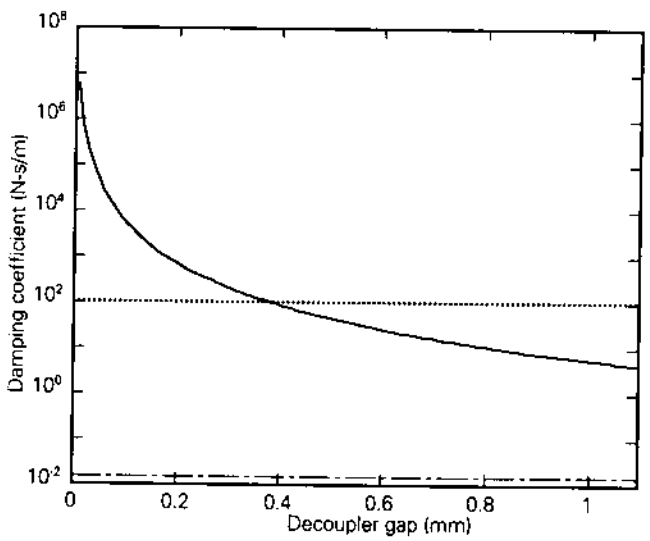

Fig. 10– Comparison of squeeze film and viscous damping coefficients for a free decoupler. Key: — b_s, ···· b_1, ···· b_{vr}.

and processed separately in both time and frequency domains. This allows us to define the following corresponding to the excitation $x(t) = X \sin(2\pi ft)$ as:

$$F_T(t) = |F_{T1}|\sin(2\pi f + \phi_1) + |F_{TH}|\sin(\pi f + \phi_H) + \sum_{j=2}^{N} |F_{Tj}|\sin(2\pi jf + \phi_j)$$

where the super-harmonics are given by the Fourier expansions from $j = 2$ to N, and the half-order sub-harmonic is denoted by subscript H. Typical results will be presented in section 9-C.

8. NONLINEAR SIMULATION MODEL

A. Decoupler switching dynamics

In the free decoupler model, the motion of a free-floating decoupler disk (Fig. 8) is described as:

$$\ddot{x}_d(t) = \begin{cases} 1/m_d\left[A_d\left[p_2(t) - p_1(t)\right] - b_v\dot{x}_d(t)\right] & ; \text{ for } 0 < x_d(t) < \delta_d \\ 0,\ \dot{x}_d(t) = 0; & \text{when } x_d(t) = 0 \text{ and } x_d(t) = \delta_d. \end{cases} \tag{9}$$

This approach is similar to the kinematic switching analysis used by Kim and Singh to predict the time events corresponding to decoupler opening or closing.[2] The case of a fixed decoupler is easily simulated by assuming $q_d = 0$.

B. Simulation issues

Based on the proposed model and identified parameters, a nonlinear simulation model is developed in the Matlab/Simulink environment. A number of sub-systems introduce nonlinearities. Except for the decoupler, all other nonlinear systems can be modeled by continuous functions that are obtained either experimentally or by the mathematical models of physical processes. Some of these continuous nonlinearities can be linearized if the dynamic excursion range is small. This holds true for $p_2(t)$ as it is close to p_a. Also, $p_1(t)$ shows significant changes because of bi-linear stiffness. While the nonlinear parameters are linearized in the linear model, a polynomial curve-fit is employed to find the nonlinear functions of relevant variables. The nonlinear simulation model is solved by employing the 4th order Runge-Kutta method with a fixed time step.[10] The total time to run the steady state simulation model for a particular X and f is specified by $60/f$. Of the $60/f$ time span, the first $40/f$ duration is used to settle down the transients associated with initial conditions. Data from the rest of the time ($20/f$) are used for both time and frequency domains predictions. The free decoupler model consumes more time due to the additional nonlinear dynamics of the decoupler mechanism.

9. COMPARISON BETWEEN THEORY AND EXPERIMENT

A. $\tilde{K}(f,x)$ Spectra

Figure11 shows measured and predicted $\tilde{K}$ for the fixed decoupler mount case corresponding to X = 0.15, 0.25, 0.5, 0.75, 1.0, 1.25, and 1.5 mm. Here f varies from 2.5 to 50

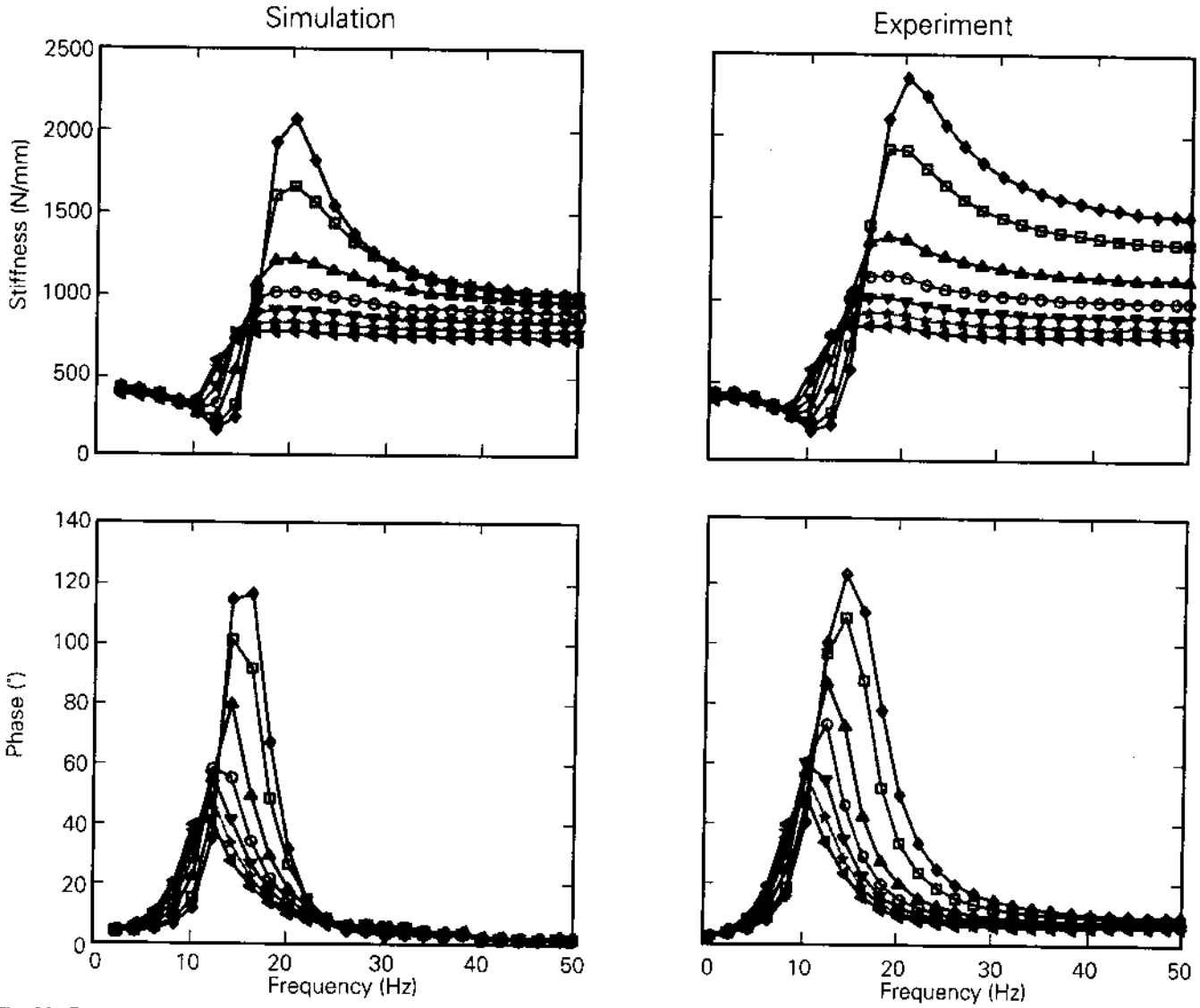

Fig. 11–Dynamic stiffness spectra of the fixed decoupler mount. Key: ◇ X=0.15mm, □ X=0.25 mm, △ X=0.5 mm, ○ X=0.75 mm, ▽ X=1.0 mm, ★ X=1.25 mm, ◁ X=1.5 mm.

Hz. Both predicted and measured results show that as the frequency increases, K and ϕ decrease, and their peaks, ($\hat{f}_K$ and $\hat{f}_\phi$) shift slightly to lower frequencies. Our simulation describes the measured results very well, with the exception of X = 0.15 and 0.25 mm at frequencies higher than 20 Hz, for which the predicted K decays faster than the measured K. For these two cases (X = 0.15 and 0.25 mm), the measured K ≈ 1500 N/mm at 40-50 Hz, while the predicted K ≈ 1200 N/mm. Discrepancies between experiment and theory, however, are primarily due to the high frequency dynamics such as turbulence and unmodeled nonlinearities. Other sources of error are associated with simplifications or assumptions made in various sub-component models.

For the free decoupler mount, the small amplitude response caused by the decoupler mechanism can be distinctly distinguished from the $\tilde{K}$ spectra of Fig. 12. As expected, for smaller amplitudes of displacement (such as X = 0.15 mm), K and ϕ of the hydraulic mount do not show significant spectral variation, like a conventional rubber mount. For this case, the decoupler remains open at all times maintaining low chamber pressures. Thus, the effective stiffness is essentially that of the rubber element. At higher amplitudes ($X \geq 0.5$ mm) the hydraulic mount is expected to behave similarly to the fixed decoupler mount since the decoupler remains closed most of the time, and the fluid flows mostly through the inertia track. Both predicted and measured $\tilde{K}$ spectra clearly show both small and large amplitude responses. For the case of X = 0.15 mm, two peaks are seen at 8.5 and 32.5 Hz in the predicted K spectrum, but these are not seen in the measured results. At these frequencies, the decoupler remains closed for some time, but the damping force is too small to keep the decoupler open. When X = 0.25 mm, an interesting phenomenon occurs. The dynamic stiffness behaves neither like the small amplitude response, nor like the large amplitude response. From Fig. 12, the measured K shows peaks at 10.5, 18.5, and 24.5 Hz, but it is relatively flat at other frequencies. Based on discussions with the mount manufacturer,[11] we conclude that 0.5 mm is very close to decoupling the input displacement. Consequently, the

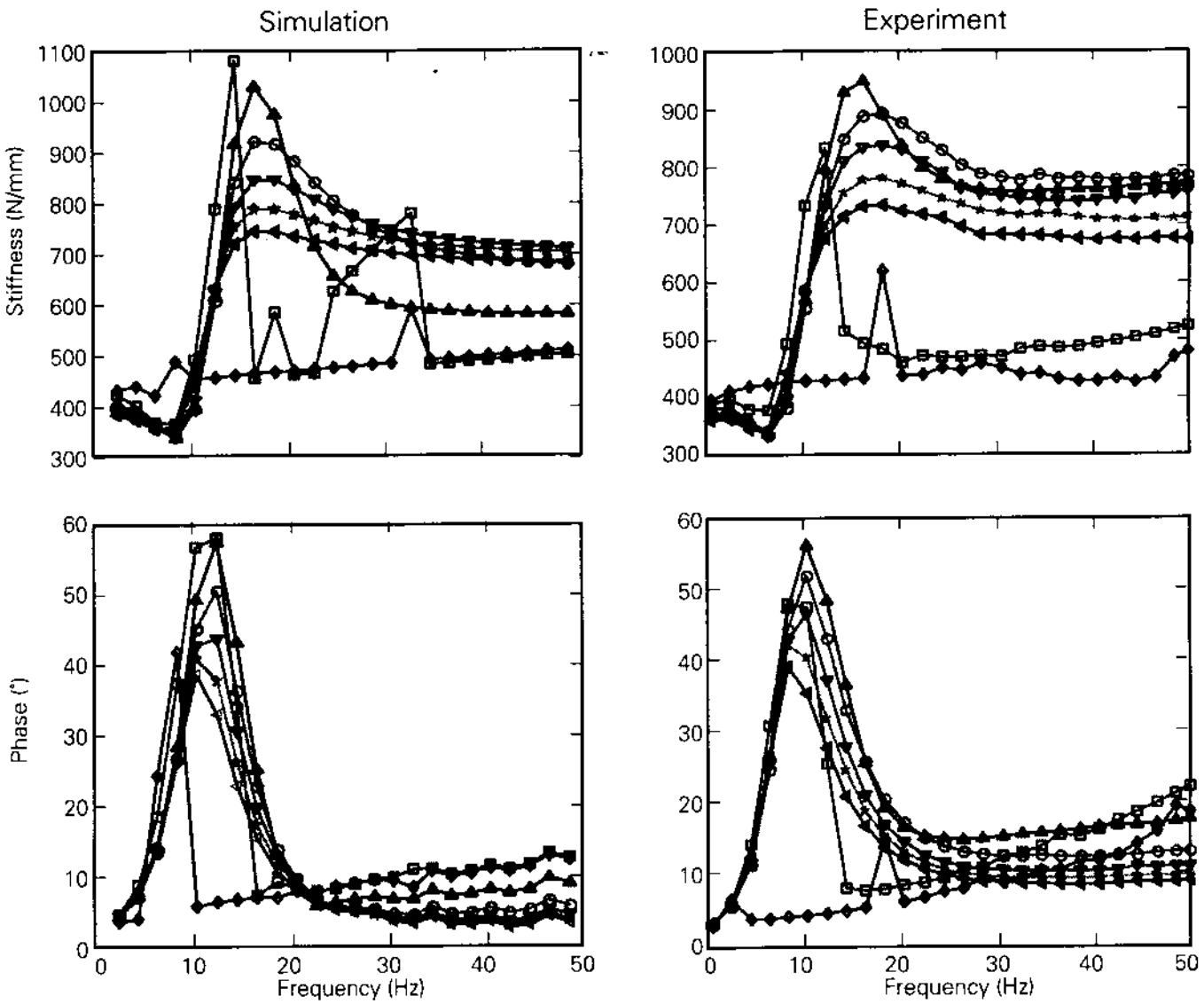

Fig.12- Dynamic stiffness spectra of the free decoupler mount. Key: ◇ X=0.15mm, □ X=0.25 mm, △ X=0.5 mm, ○ X=0.75 mm, ▽ X=1.0 mm, ★ X=1.25 mm, ◁ X=1.5 mm.

decoupler starts to close at some frequencies and as a result yields a higher K. Similarly, it opens up at other frequencies and results in a lower rate. Other experimental tests show good repeatability for both fixed and free decoupler mounts.

B. Peak-to-peak transmitted force and top chamber pressure

Since the $\tilde{K}(f,x)$ spectra present results only at the excitation frequency f, the peak-to-peak F_T and p_t values (based on time domain responses) are also plotted in a spectral form for better comparison. Figure 13 shows that predicted F_T and p_t agree well with measured results, both in terms of magnitudes and trends, though predictions are slightly higher than measurements. For the free decoupler mount at 18 Hz, measured spectra show a peak in both F_T and p_t. This suggests that the small amplitude response might be intended for $X <$ 0.15 mm, where the decoupler will not close at all. From the measured and predicted plots (Figs. 12 and 13), one could infer that the system exhibits a softening type nonlinearity. As X is increased, the peaks in $F_{p\text{-}p}$ and $\phi_{p\text{-}p}$ move to lower frequencies.

C. Steady-state time domain responses

Although the frequency domain simulations match well with measurements, a more important and yet difficult task in the model validation process is to compare time domain responses, especially when nonlinearities introduced by vacuum formation and the decoupler mechanism are of interest. Only the free decoupler case is reported here and the decoupler disk actions may be viewed via $p_t(t)$ and its comparison with $F_T(t)$. The dynamic pressure transducer capable of recording only beyond 0.5 Hz, yields much cleaner, low noise p_t signals when compared with the absolute pressure transducer. However the static pressure for the chamber can

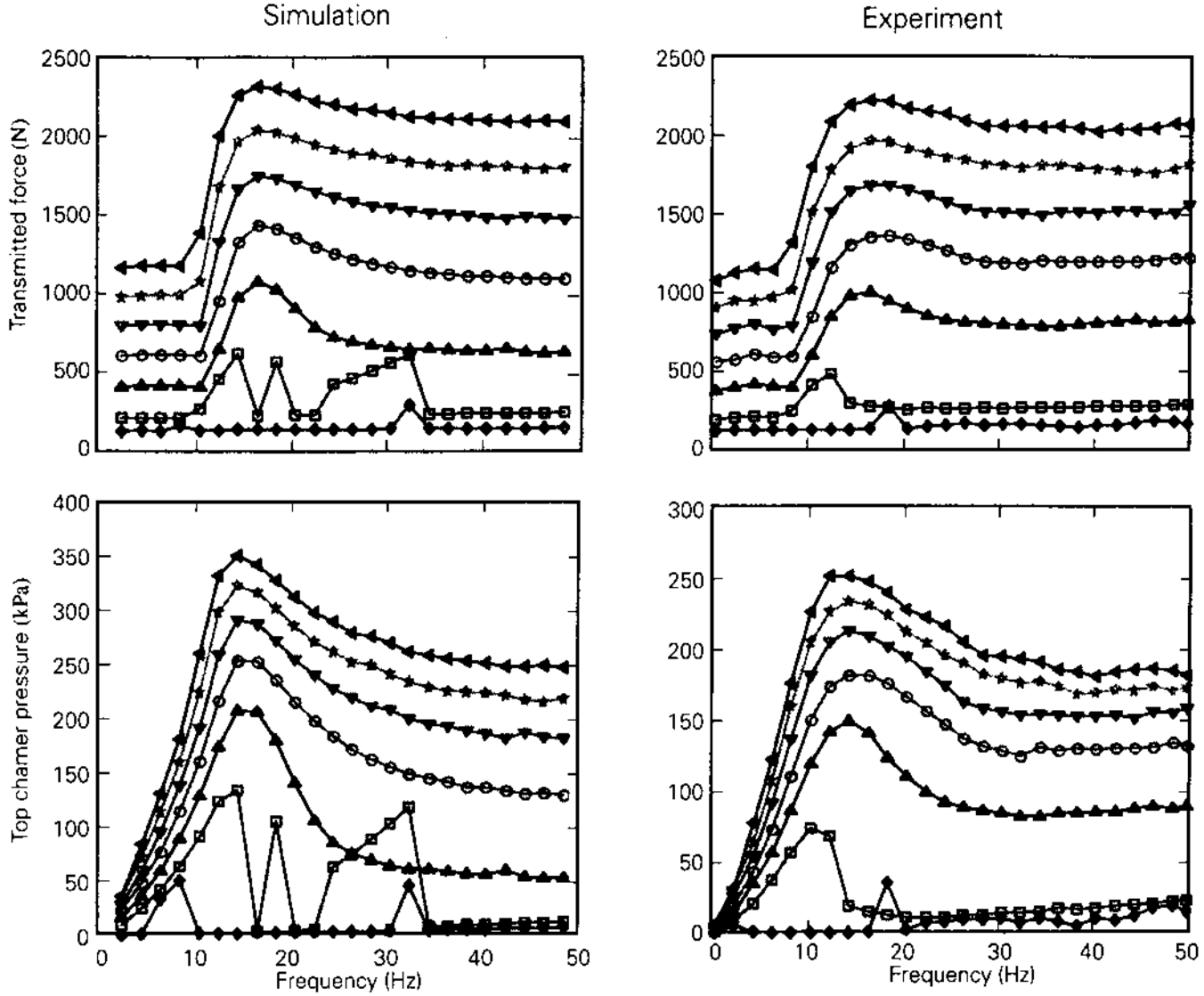

Fig. 13–Peak to peak values of transmitted force and top chamber pressure of the free decoupler mount. Key: ◇ X=0.15mm, □ X=0.25 mm, △ X=0.5 mm, O X=0.75 mm, ▽ X=1.0 mm, ★ X=1.25 mm, ◁ X=1.5 mm.

be measured with the absolute pressure transducer only.

Figures 14 and 15 compare predicted and measured F_T and p_1 given different f and X. Figure 14 shows the decoupler action causes a drastic change in p_1. Opening the decoupler at low f induces p_1 and p_2 to become nearly equal and approach p_a. This yields a prominent flat region in $p_1(t)$ corresponding to nearly zero gage pressure p_a. Measured results and simulations agree well.

When $X = 0.15$ mm, predicted p_1 seems to be harmonic, and its amplitude is small since the decoupler remains open at all times. For $X = 0.15$ and 0.25 mm at 20.5 Hz, measured $p_1(t)$ shown in Fig. 15 shows that the higher frequency dynamics, not modeled here, is caused by the "dithering" action of the decoupler disk. However, the magnitude of p_1 is so low that it does not much affect F_T. Since the design specification is often in terms of F_T and not p_1, one has to judge as to how accurate the decoupler model needs to be, considering the complexities introduced by a discontinuous nonlinearity.

At higher X values (0.5, 1.0, and 1.5 mm), some fluctuations are also seen in the measured p_1 when the decoupler acts. These fluctuations suggest that the damping force acting on the decoupler is not constant; instead it could be a function of X and/or f. At high f and X, the peak-to-peak p_1 of Fig. 15 changes rapidly since the decoupler opens quickly and does not allow pressure equalization. The waveform of Fig. 15 does not have the prolonged flat portion as seen at low frequencies in Fig. 14, but develops bumps on the sides. Strong vacuum formation takes place, resulting in a distortion of $p_1(t)$.

D. Super- and sub-harmonics

For a fixed decoupler mount, the non-sinusoidal responses to a sinusoidal displacement input are dictated by the presence of vacuum in the top chamber. We can clearly observe this from measured distorted p_1 waveform as shown in Fig. 16. In most of the cases where the nonlinearities due to vacuum exist, the super-harmonic terms such as $2f$, $3f$, $4f$, etc. in p_1 and F_T are

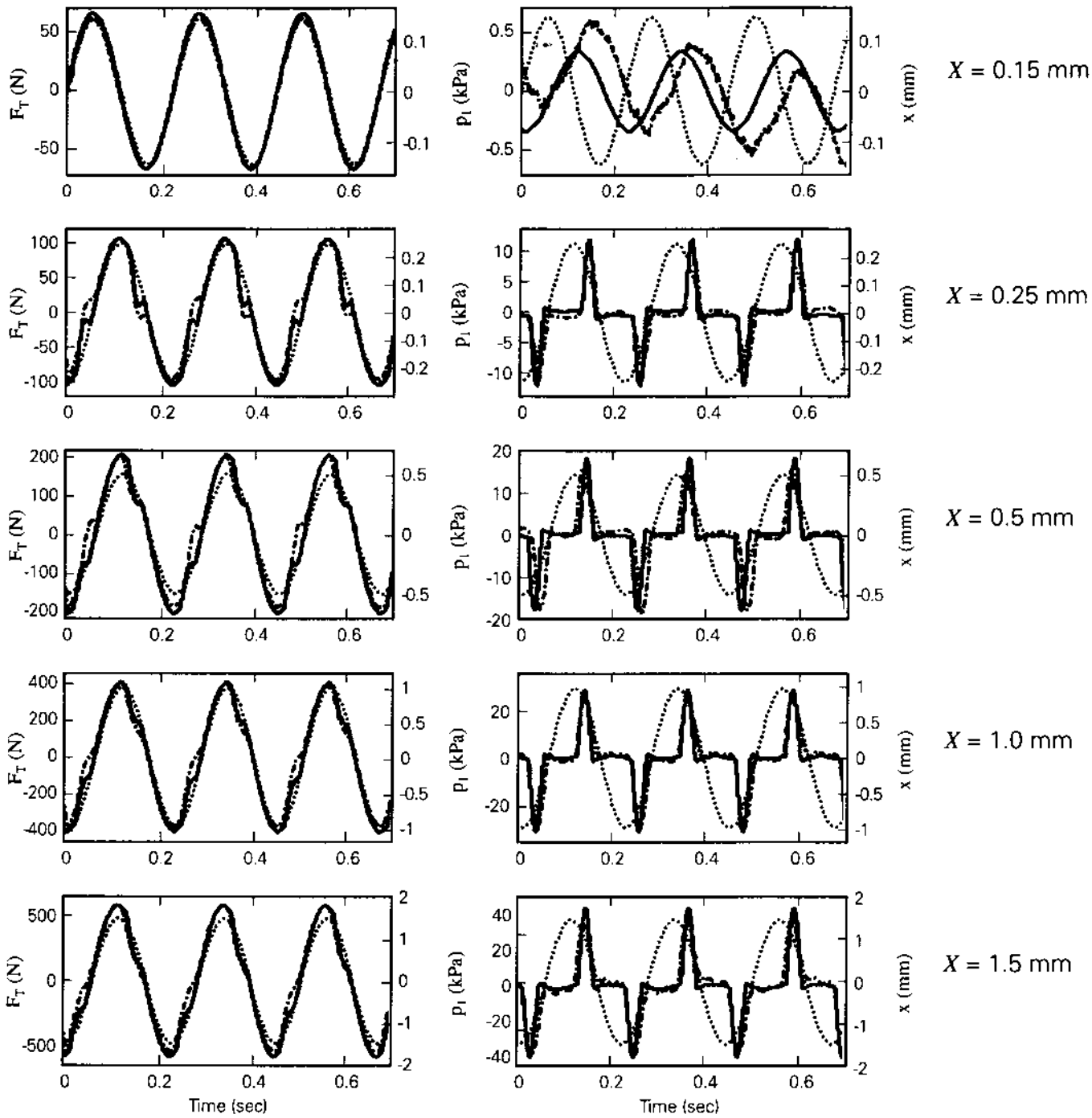

Fig. 14– Predicted and measured steady-state time domain response of the free decoupler mount at 4.5 Hz. Key: — Simulation (F_T and p_l), -·- Measured (F_T and p_l), ···· x.

very dominant. Also, some *f*/2, 3*f*/2, 5*f*/2 and the like terms appear when $f = 28$ Hz to 32 Hz. These could very well be the combination frequencies where the fundamental frequency is f and the sub-harmonic is $f/2$. Simulated time histories and FFT spectra also show this phenomenon very clearly (Figs. 17 and 18).

For a free floating decoupler mount, the mount acts like a conventional rubber mount for small X due to the decoupler mechanism, and hence the response of the mount is almost linear. For large X, nonlinearities due to both the presence of vacuum and the decoupler switching mechanism result in super-harmonic contents. Note that sub-and super- harmonic (non-resonant) components are mainly due to a large forced response amplitude. Analyses similar to that of Refs. 12 and 13 will need to be undertaken for a better understanding of the non-linear effects.

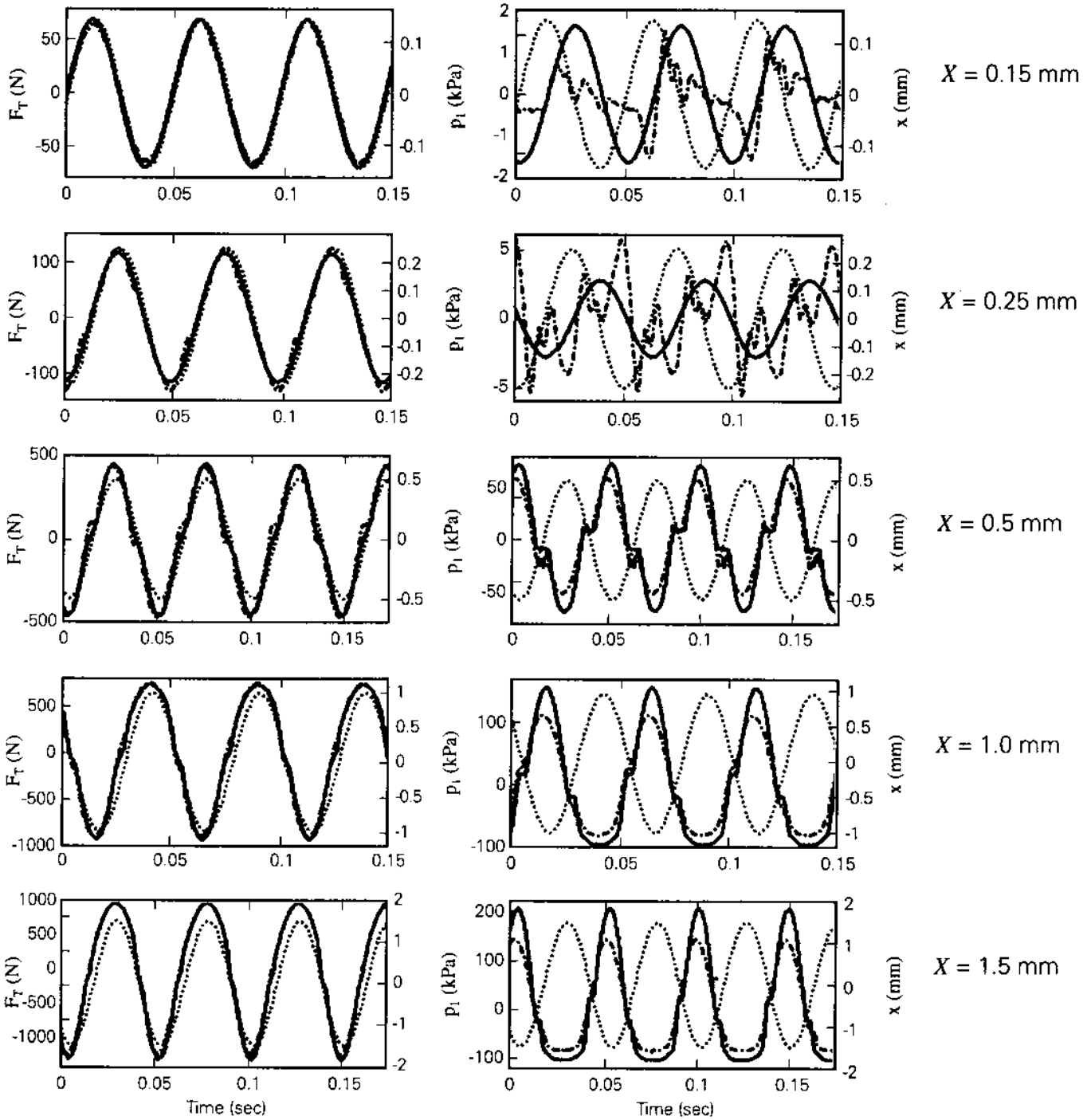

Fig. 15– Predicted and measured steady-state time domain response of the free decoupler mount at 20.5 Hz. Key: — Simulation (F_T and p_1), --- Measured (F_T and p_1), ···· x.

10. CONCLUSION

A hydraulic engine mount with an inertia track and a free-floating decoupler has been investigated experimentally. To better observe the contribution of the fluid component to the dynamics of the overall system, absolute and dynamic pressure transducers are installed in the top chamber to examine the static and dynamic fluid pressure respectively. Bench experiments are constructed to identify various mount parameters such as inertia track resistance, top and bottom chamber compliances, and effective piston area of the top chamber. Measurements show that the top chamber compliance varies significantly with the preload. These bench experiment results are also critical in providing the necessary input to the Matlab/Simulink based simulation model. A new model of the decoupler based on an equivalent viscous damping mechanism concept is used. The decoupler model accurately predicts the events related to the decoupler openings and closings. This is a key achievement since the decoupler action significantly

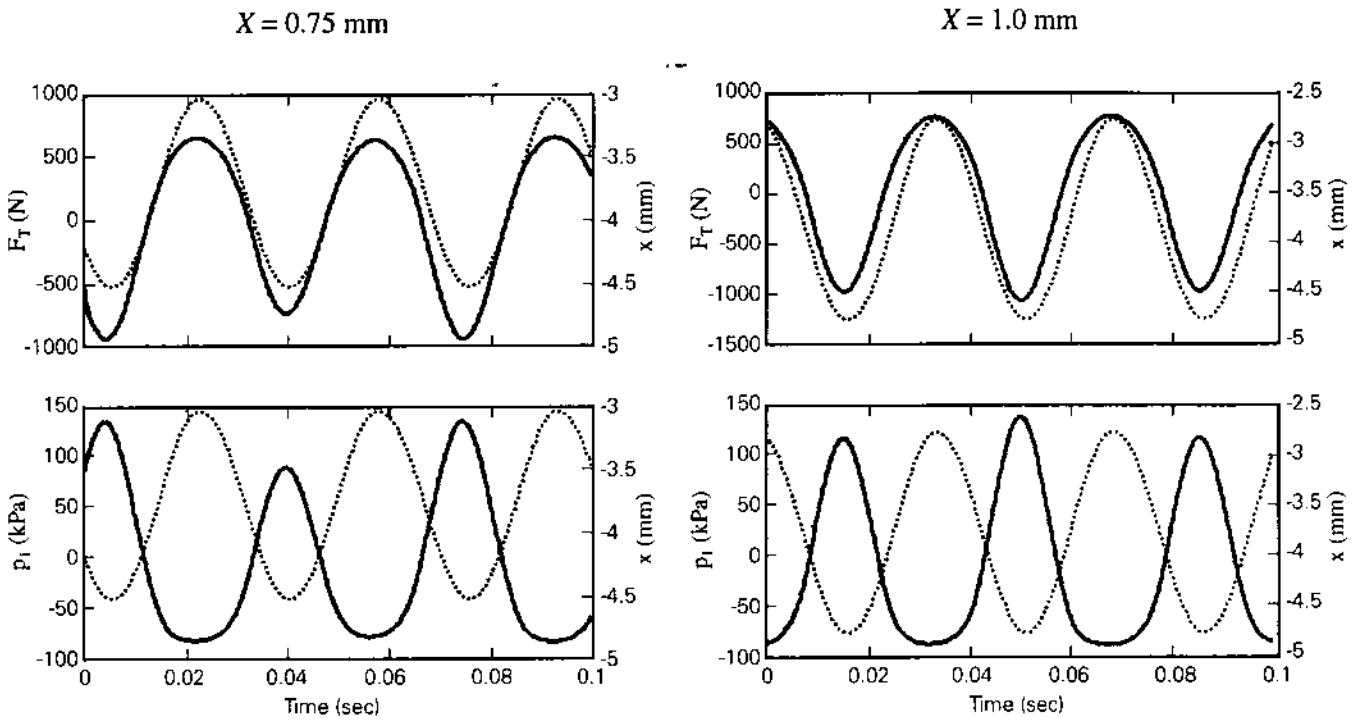

Fig. 16– Sub-harmonic contents observed in experimental results given excitation at 28.5 Hz. Key: — F_T or p_l, ···· x.

affects the fluid pressures within the chambers and thus the mount stiffness. Applying a standard steady state dynamic characterization test procedure, the nonlinear dynamics due to the decoupler switching mechanism and vacuum in the top chamber are clearly seen in time domain histories. The super-harmonic content in the response is seen in most of the cases, but at certain frequencies and amplitudes both sub- and super-harmonics are simultaneously present. Finally, future work should attempt to better understand the nonlinear mechanisms, though our model predicts the experimental results reasonably well both in time and frequency domains.

11. ACKNOWLEDGMENT

We gratefully acknowledge the financial support from the Ford Motor Company. Equipment grants from the Ohio Board of Regents and the MTS Systems Corporation made the experimental work possible. Thanks are also extended to Delphi Automotive (Chassis) for providing the mount components.

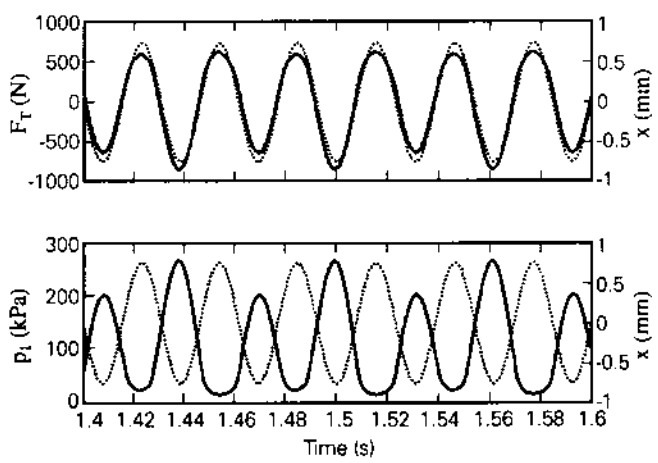

Fig. 17– Sub-harmonic contents shown in the simulated time domain responses given X = 0.75 mm and f = 32.5 Hz. Key: ——— F_T or p_l, ····· x.

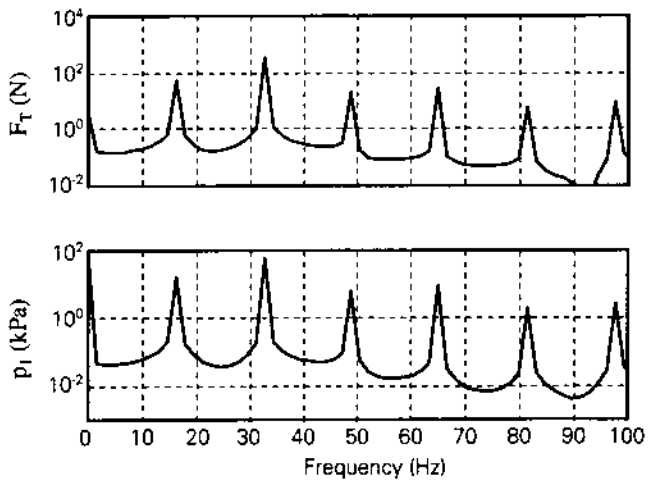

Fig. 18– Sub-harmonic (f/2) and multiples observed in the simulated FFT plots given X = 0.75 mm and excitation frequency f = 32.5 Hz.

12. REFERENCES

[1] MTS Systems Corporation, *TestStar II Control System Reference Manual* (1999).

[2] G. Kim and R. Singh, "Study of Passive and Adaptive Hydraulic Engine Mount Systems with Emphasis on Nonlinear Characteristics," J. Sound Vib. **179**(3), 427-453 (1995).

[3] R. Singh, G. Kim, and P. V. Ravindra, "Linear Analysis of Automotive Hydro-mechanical Mount with Emphasis on Decoupler Characteristic," J. Sound Vib. **158**(2), 219-243 (1992).

[4] J. E. Colgate, C. T. Chang, Y. C. Chiou, W. K. Liu, and L. M. Keer, "Modelling of a hydraulic engine mount focusing on response to sinusoidal and composite excitations," J. Sound Vib. **184**(3), 503-528 (1995).

[5] T. Jeong, "Analysis of powertrain mounts with focus on torque roll axis decoupling and frequency-dependent properties," Ph.D. Dissertation, The Ohio State University (2000).

[6] G. Kim and R. Singh, "Nonlinear Analysis of Automotive Hydraulic Engine Mount," ASME J. Dynamic Systems, Measurement and Control **115**, 482-487 (1993).

[7] E. O. Doebelin, *System Dynamics: Modeling, Analysis, Simulation, Design* (Marcel Dekker, Inc., New York, 1998).

[8] A. Cameron, *Basic Lubrication Theory* (Longman Group Ltd, New York, 1970).

[9] R. W. Fox and A. T. McDonald, *Introduction to Fluid Mechanics*, (John Wiley & Sons, Inc., New York, 1992).

[10] Mathworks, Inc., *Learning SIMULINK version 3.0* (1999).

[11] S. Tewani, Delphi Chassis, *Personal Communication* (2000-01).

[12] T. J. Royston and R. Singh, "Study of Nonlinear Hydraulic Engine Mounts Focusing on Decoupler Modeling and Design," SAE 1997 Trans.—Journal of Passenger Cars **106**, 2759-2769 (1998).

[13] T. J. Royston and R. Singh, "Vibratory Power Flow Through a Nonlinear Path into A Resonant Receiver," J. Acoust. Soc. Am. **101** (4), 2059-2069 (1997).